



## Full Length Article

# Photocatalytic hydrogen evolution of palladium nanoparticles decorated black TiO<sub>2</sub> calcined in argon atmosphere



Ming-Chung Wu<sup>a,b,c,\*</sup>, Kai-Chi Hsiao<sup>a</sup>, Yin-Hsuan Chang<sup>a</sup>, Shun-Hsiang Chan<sup>a</sup>

<sup>a</sup> Department of Chemical and Materials Engineering, College of Engineering, Chang Gung University, Taoyuan, 33302, Taiwan

<sup>b</sup> Green Technology Research Center, Chang Gung University, Taoyuan 33302, Taiwan

<sup>c</sup> Division of Neonatology, Department of Pediatrics, Chang Gung Memorial Hospital, Taoyuan 33305, Taiwan

## ARTICLE INFO

## Article history:

Received 20 May 2017

Received in revised form 3 August 2017

Accepted 9 August 2017

Available online 16 August 2017

## Keywords:

Hydrogenation

TiO<sub>2</sub>

Photocatalytic hydrogen production

Photodegradation

Sol-gel method

## ABSTRACT

Black TiO<sub>2</sub> nanoparticles (BTN) was prepared by sol-gel derived precursor calcined in an argon atmosphere. The synthesized BTN with trivalent titanium ion, structural defect, and oxygen vacancy shows a remarkably high absorbance in the visible light spectrum. BTN thus behaves a higher visible-active nanoreactor than white TiO<sub>2</sub> nanoparticles (WTN) in the aqueous solution for organic pollutant degradation. Moreover, palladium decoration on the BTN surface (Pd-BTN) demonstrates a fascinating clean energy application. The obtained Pd-BTN fulfills a satisfied green material demand in the photocatalytic hydrogen production application. Pd-BTN calcined at 400 °C (Pd-BTN-400) shows the high photocatalytic hydrogen generation rate of 5200 μmol/g h under UV-A irradiation and 9300 μmol/g h under UV-B irradiation, respectively. The well-developed material, Pd-BTN-400, could be one of the best solutions in the concern of clean energy and water-purification with regard to the continuous environmental issue.

© 2017 Elsevier B.V. All rights reserved.

## 1. Introduction

Photocatalysts have received intense attention for the pollutant degradation and clean energy applications [1–6]. The most commonly used photocatalyst is environmental friendly TiO<sub>2</sub> nanoparticles [7–9]. It is an inexpensive material not only easy to produce and to use, but also thermally and chemically stable. However, a significant disadvantage is arisen because of its broad bandgap (anatase phase ~3.2 eV; rutile phase ~3.0 eV) only located in ultraviolet absorption [10,11]. How to improve the utilization rate of solar light to increase the absorption efficiency has been considered as an emerging challenge topic for scientists. The recent discovered “black TiO<sub>2</sub> nanoparticles” (BTN) has gathered many interests for its visible light absorption capability [12–14]. BTN was derived from anatase TiO<sub>2</sub> calcined at 200 °C for 5 days under 20 bar hydrogen atmosphere. The hydrogen reduction process [15–18] or the oxidation process [19], as well as other reduction methods [20,21], were developed to produce the disorder-engineered BTN. The hydrogenated treatment causes the lattice disorder in TiO<sub>2</sub> nanoparticles based on the highly localized

midgap states that result in the electrons and holes separation [22]. BTN with low bandgap also can be obtained by a one-step reduction/crystallization procedure [23–25]. All of them aims to perform high photocatalytic activities, including the photocatalytic hydrogen generation and the photocatalytic degradation of organic dyes [12,13]. Even though BTN has boosted the high visible absorption, the visible active photocatalytic characteristic is still unsatisfactory because the short lifetime of photoinduced electron and hole [26]. Hydrogen treatment thus becomes an effective method to enhance the performance of highly photo-active hydrogenated TiO<sub>2</sub> for photo-electrochemical water splitting [27–29].

Many literatures have been reported towards the improvement of the absorption behavior such as doping metal or non-metal into TiO<sub>2</sub>, and decorating nano-metallic on the surface of TiO<sub>2</sub>. Using metal or non-metal as dopants can tune the edge of valence band or conduction band which can thus widen absorption band from UV to visible light [30–33]. The photocatalytic characteristics of metal-doped TiO<sub>2</sub> or nonmetal-doped TiO<sub>2</sub> substantially are based on the dopant, the doping concentration, synthesis method, and its calcination process [34–40]. Loading cocatalyst on the photocatalysts surface as the heterojunction structure is an efficient method to facilitate the photocatalytic hydrogen generation [41–46]. Hence, many research has focused on the metal decorated TiO<sub>2</sub> to obtain the high active photocatalysts [47–50]. The co-catalyst acts as the electron acceptor so that the transfer of photoinduced electron can be facilitated [51–54]. With the improved separation of the

\* Corresponding author at: Department of Chemical and Materials Engineering, College of Engineering, Chang Gung University, Taoyuan, 33302, Taiwan.

E-mail addresses: [mingchungwu@mail.cgu.edu.tw](mailto:mingchungwu@mail.cgu.edu.tw), [mingchungwu@ntu.edu.tw](mailto:mingchungwu@ntu.edu.tw) (M.-C. Wu).

electron-hole pair, the photocatalytic H<sub>2</sub> generation can thus be increased. For proper nano-metallic decoration sizes, the localized surface plasma resonance (LSPR) could be induced to enhance optical properties in visible region [55–59].

As mentioned, black TiO<sub>2</sub> was usually synthesized under the high hydrogen pressure atmosphere followed by a long calcination process. Due to the danger of flammable hydrogen, the synthesis process with high hydrogen pressure has raised public safety worries [60,61]. The objective of this study is to obtain a Pd-BTN with high photocatalytic activity in a moderate secure process [53,62,63]. At first, we prepared the BTN by sol-gel method with thermal treatment under an argon flow. The Pd nanoparticle was deposited onto the BTN surface by wet impregnation method to increase the electron hole pair separation. We first explored the BTN characteristic and utilized BTN as a nanoreactor for photodegradation of methyl orange to simulate the photodegradation of pollutants. The visible-active photodegradation performance is correlated to the absorption behavior of BTN series. The obtained Pd-BTN could be a potential alternative for the commercial photocatalyst applied in the field of photodegradation pollutant and photocatalytic H<sub>2</sub> generation.

## 2. Experimental details

Ti-O precursor gel was fabricated by the sol-gel process. In the beginning, 7.20 mL titanium isopropoxide (Ti(OCH(CH<sub>3</sub>)<sub>2</sub>)<sub>4</sub>, ACROS, 98 +%) and 21.60 mL *n*-propanol (C<sub>3</sub>H<sub>7</sub>OH, Fisher, reagent grade) were mixed well at room temperature. Then, 1.00 mL hydrochloric acid (HCl, ACROS, 37%) and 1.00 mL deionized water are added to initiate the gelation process. After that, the Ti-O precursor gel was calcined at various temperatures (350, 400, 450, 500, 550, and 600 °C) under air flow (21% O<sub>2</sub> in N<sub>2</sub>) or argon flow (99.995%) for 2 h. Finally, we obtained a series of white TiO<sub>2</sub> nanoparticles (WTN) and BTN. For the Pd decoration onto the surface of TiO<sub>2</sub> NFs, we suspended 14.6 mg of palladium(II) acetylacetonate (Aldrich, 99%) and 500 mg of the as-prepared WTN series and BTN series into 100 mL of acetone (ACROS, 99.5 +%) and mixed well by the ultrasonic bath for 3 h. After that, we kept the mixture stirring for 12 h and subsequently evaporated at ~80 °C. The samples were kept calcined under an H<sub>2</sub>/N<sub>2</sub> atmosphere at 300 °C for 4 h. Eventually, we obtained WTN series and BTN series loaded with 1.00 wt% palladium, which denotes as Pd-WTN-X and Pd-BTN-X, respectively.

The Kubelka-Munk function,  $F(R)$ , spectra of WTN series and BTN series were analyzed by the UV/Vis spectrophotometer (Jasco, V-650, Japan) recorded from 260 to 800 nm wavelength. The crystal structures of WTN series and BTN series were observed by X-ray diffractometer (XRD, Bruker, D2 phaser with Xflash 430, Germany). X-ray photoelectron spectroscopy spectra were measured and recorded by X-ray photoelectron spectrometer system (K-Alpha, Thermo Fisher Scientific) using micro-focused Al K $\alpha$  X-ray source. The microstructures of BTN-400 and Pd-BTN-400 were observed by field-emission transmission electron microscope (FT-TEM, JEM-ARM200FTH, Japan). Brunauer-Emmett-Teller (BET) surface area was investigated by an accelerated surface area and porosimetry system (ASAP 2010, Micromeritics).

For the measurement of the photodegradation of methyl orange, each 20.0 mg of WTN series or BTN series was dispersed in 150.0 mL methyl orange aqueous solution (~10.0 mg/L) at ambient conditions. The three kinds of light sources we adopted included UV-B light (Sankyo Denki, G15T8E,  $\lambda_{\max}$  ~312 nm, 8.0 W), UV-A light (Sankyo Denki, G8T5BLB,  $\lambda_{\max}$  ~352 nm, 8.0 W), and visible light (Goodly, F8T5/D, 8.0 W). They were placed above the reaction system top around ~10.0 cm. Before the photodegradation experiment, the suspensions have been put in the dark for 0.5 h to achieve the adsorption equilibrium and thus minimize the surface

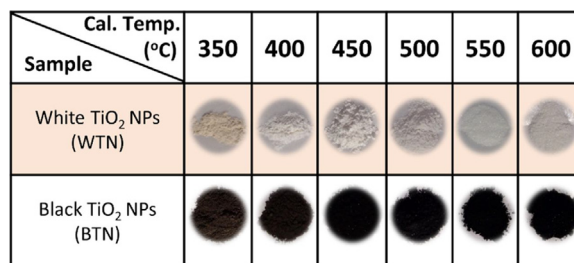


Fig. 1. Camera images of different synthesized WTN and BTN calcined at various temperatures of 350, 400, 450, 500, 550 and 600 °C for 2 h.

adsorption behavior. The suspension of retained methyl orange was centrifuged, and its concentration was estimated by UV/Vis spectrophotometer recorded from the 300–800 nm wavelength. By comparing the intensity of the methyl orange characteristic peak located at  $\lambda = 464$  nm with the calibration curve examined previously, we can obtain its corresponding concentration.

Photocatalytic hydrogen production measurement takes place in the 2.0 L mixture of C<sub>2</sub>H<sub>5</sub>OH and H<sub>2</sub>O with the volume ratio of 1.0:1.0. Fifty milligrams Pd-BTN was suspended well in the mixture aqueous solution by the ultrasonic bath. The three kinds of light sources were applied in the photocatalytic hydrogen production measurement. The six pieces of lamps were placed around the reactor in a hexagonal arrangement, and the distance between the reactor and the lamp is ~5 cm. Aiming to avoid the sedimentation of Pd-BTN, nitrogen (99.995%) was bubbled into the reaction system. Nitrogen also acted as the carrier gas for the photogenerated hydrogen products, and its flow rate is controlled at 400 mL min<sup>-1</sup> by a mass flow meter (C100L, Sierra). The liquid nitrogen cold trap system and the molecular sieve were connected to the outlet of the reaction system to diminish the vapor of C<sub>2</sub>H<sub>5</sub>OH and H<sub>2</sub>O. Finally, the photocatalytic hydrogen generation rate was recorded by a Status FGD3 gas detector [63].

## 3. Results and discussion

Aiming to optimize the calcination temperature that produces the highly photocatalytic active TiO<sub>2</sub>, the synthesized Ti-O precursor gels were calcined under the flow of air or argon. The synthesized Ti-O precursor gels calcined under the flow of air or argon at different temperatures for 2 h are denoted as WTN-X and BTN-X, respectively, where X indicates the calcination temperature. Camera images of different synthesized WTN series and BTN series are shown in Fig. 1. For WTN calcined at 350 °C, its color is gray and brown caused by the existence of carbon. When the calcination temperature is above 400 °C, WTN presents powder style in white color. For BTN series, the color of BTN became black as the calcination temperature above 400 °C. The Kubelka-Munk function spectra,  $F(R)$ , of both WTN series and BTN series are shown in Fig. 2. Interestingly, WTN series only showed absorption behavior in UV range (Fig. 2(a)). The  $F(R)$  spectra of BTN series present an obvious absorption in visible light band ranged from 400 ~ 800 nm compared with WTN-X series (Fig. 2(b)). For WTN series, the  $F(R)$  spectra of WTN-550 and WTN-600 extend to visible range due to the formation of rutile TiO<sub>2</sub>. For BTN series, the  $F(R)$  of BTN-550 is the highest among other. However, BTN-600 shows the decreased absorption on account of the formation of rutile TiO<sub>2</sub> in BTN. The  $F(R)$  spectra clearly extended to the visible range since the Ti-O precursor gel was calcined in argon. We suppose that the bandgap of BTN series decrease as the structural defects occur in the TiO<sub>2</sub> lattice after the argon calcination process.

Both WTN series and BTN series were analyzed by X-ray diffractometer to observe the crystal structure as shown in Fig. 3. For

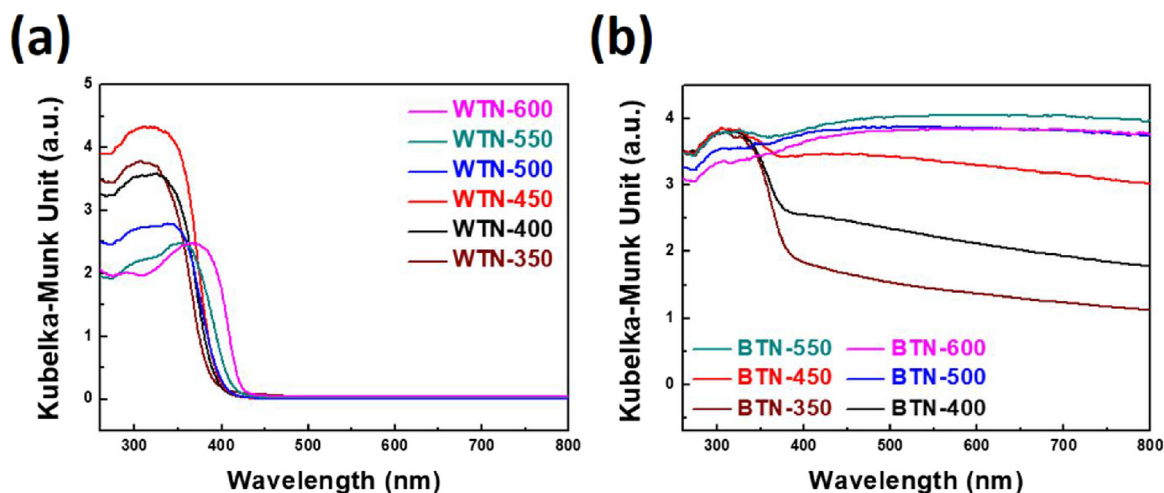


Fig. 2. Kubelka-Munk function spectra of synthesized (a) WTN and (b) BTN calcined at different temperatures of 350, 400, 450, 500, 550 and 600 °C for 2 h.

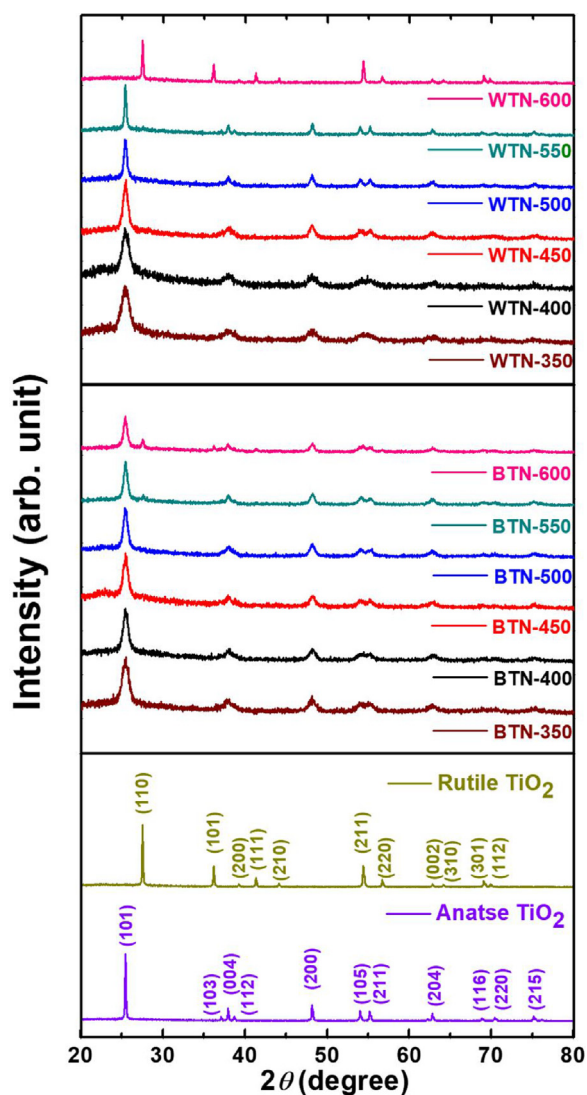
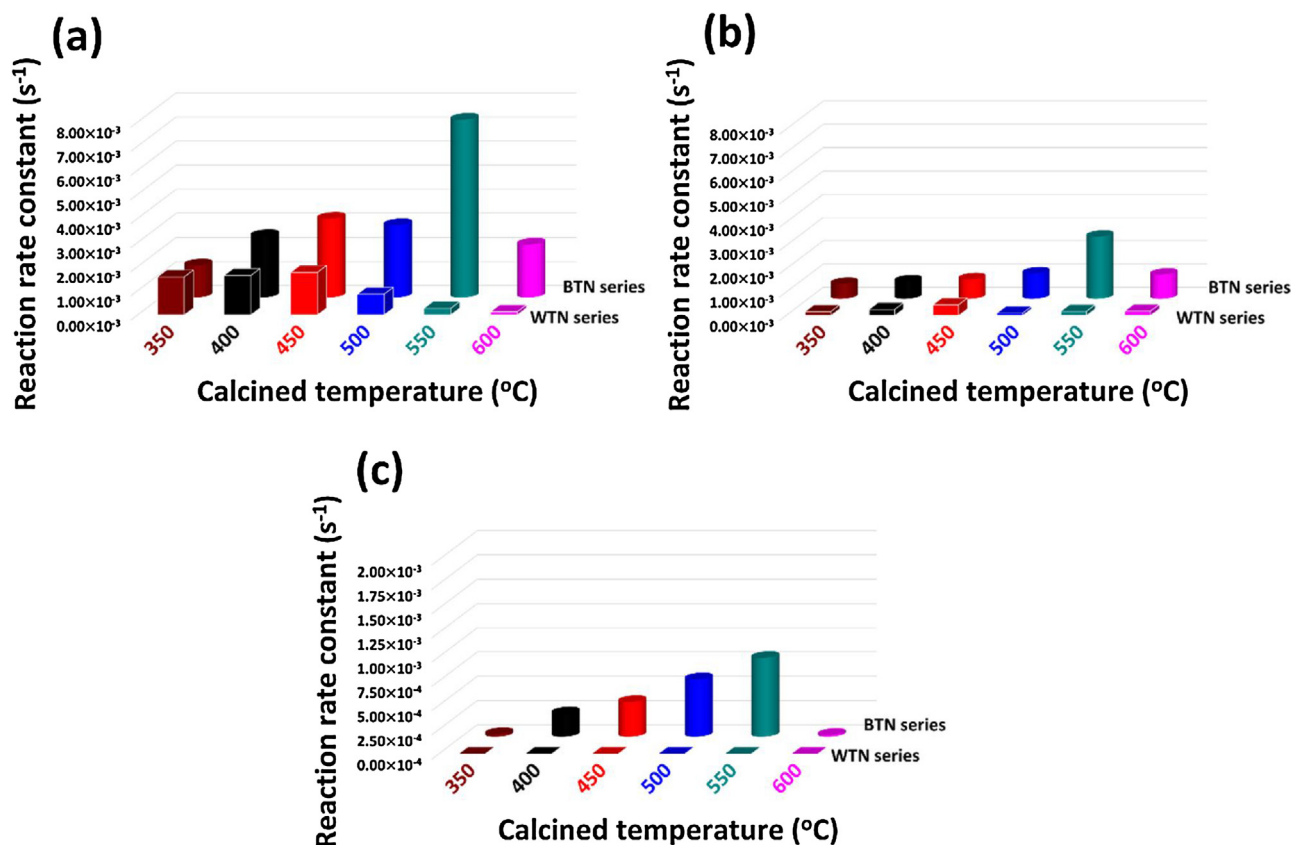


Fig. 3. X-ray diffraction patterns of WTN series and BTN series calcined at different temperatures for 2 h.

both WTN series and BTN series calcined below 500 °C, the intensity of the characteristic peak located at  $2\theta$  of 25.3° increased with the increasing calcination temperature. The results show that the ordering of anatase TiO<sub>2</sub> lattice is improved by increasing the calcination temperature. Most of the diffraction peaks are consistent with the body-centered tetragonal unit cell of anatase TiO<sub>2</sub>, and its lattice parameters are  $a = 3.78\text{Å}$  and  $c = 9.52\text{Å}$  [COD ID: 7206075] [64]. For the calcination temperature above 500 °C, BTN-550 and BTN-600 present the mixed phase involving anatase TiO<sub>2</sub> and rutile TiO<sub>2</sub>. WTN-600 only shows the single rutile TiO<sub>2</sub> phase. It is noted that the oxygen-rich environment facilitated TiO<sub>2</sub> phase to transform from anatase phase to rutile phase. XRD patterns of WTN-600 can be indexed as rutile TiO<sub>2</sub> with the lattice parameters of  $a = 4.58\text{Å}$ , and  $c = 2.96\text{Å}$  [COD ID: 4102355]. At the same calcination temperature, the calcination process in argon could hinder the formation of rutile TiO<sub>2</sub> contrasted with WTN series calcined in air. Therefore, the unique TiO<sub>2</sub> crystal structure could be formed in the specific atmospheric heat treatment.

In the present study, both WTN series and BTN series were applied to measure the photodegradation performance under different light source irradiation. In Fig. S1 and S2 of Supplementary Information, the  $C/C_0$  curves under UV-B, UV-A, and visible light irradiation with WTN series and BTN series are presented. The photodegradation test using TiO<sub>2</sub>-based material usually follows Langmuir-Hinshelwood model. The photodegradation behavior can be described as a 1st order kinetics at the low dye concentration as shown in  $\ln\left(\frac{C_0}{C}\right) = kt$ , where  $C_0$  is the initial concentration,  $C$  is the concentration at the various time,  $k$  is the reaction rate constant, and  $t$  is the photodegradation time. The slopes of each fitting lines, which using  $\ln\left(\frac{C_0}{C}\right)$  as a function of  $t$ , indicate the reaction constants of various synthesized TiO<sub>2</sub> [65,66].

The calculated reaction rate constants of both WTN series and BTN series under different light source irradiation are shown in Fig. 4. BTN series shows the higher photodegradation activity with respect to WTN series. Among them, BTN-550 shows the maximum reaction rate constant. The calculated  $k$  of BTN-550 under UV-B irradiation (Fig. 4(a)), UV-A irradiation (Fig. 4(b)) and visible light irradiation (Fig. 4(c)) are  $7.38 \times 10^{-3}$ ,  $2.67 \times 10^{-3}$  and  $8.1 \times 10^{-4} \text{s}^{-1}$ , respectively. It is noted that under visible light irradiation, WTN series with various calcination temperature show no activity. Moreover, the commercial TiO<sub>2</sub> photocatalyst – AEROXIDE® TiO<sub>2</sub> P25 is a standard material as a competitor for photodegradation test. The calculated reaction rate constants of AEROXIDE® TiO<sub>2</sub> P25 under UV-B irradiation is  $1.42 \times 10^{-2} \text{s}^{-1}$  and



**Fig. 4.** The photodegradation reaction rate constants for the synthesized WTN series and BTN series under the following light source irradiation: (a) UV-B irradiation, (b) UV-A irradiation, and (c) visible light irradiation.

UV-A irradiation is  $3.40 \times 10^{-3} \text{ s}^{-1}$ . Under visible light irradiation, AEROXIDE<sup>®</sup> TiO<sub>2</sub> P25 only shows  $2.77 \times 10^{-4} \text{ s}^{-1}$ . The calculated reaction rate constant of BTN-550 is three times higher than AEROXIDE<sup>®</sup> TiO<sub>2</sub> P25 under visible light irradiation. The BET surface area of BTN-550 is  $\sim 58.39 \text{ m}^2/\text{g}$ , which is very close to that of AEROXIDE<sup>®</sup> TiO<sub>2</sub> P25 ( $\sim 56 \text{ m}^2/\text{g}$ ) [67]. The result suggests that the higher photocatalytic activity of BTN-550 is not caused by the specific surface area, and the results might be caused by the hydrogenated process that caused the enhanced visible light absorption. Although BTN-550 shows the lower reaction rate constant than AEROXIDE<sup>®</sup> TiO<sub>2</sub> P25 under UV irradiation, it is hard to find a material with the photocatalytic performance higher than AEROXIDE<sup>®</sup> TiO<sub>2</sub> P25 under UV irradiation. Based on the photodegradation tests, it is clear that the activity is highly related to the absorption behavior.

For the photocatalytic H<sub>2</sub> generation rates of WTN series and BTN series, they show the undetectable H<sub>2</sub> value under UV-B irradiation. Although BTN series is helpful for absorbing the light ranged from UV band to visible band, the photocatalytic H<sub>2</sub> generation performance is limited by its redox potential. The lowest level of the conduction band ( $E_{CB}$ ) should be more negative than the redox potential of H<sup>+</sup>/H<sub>2</sub> (0 V vs. NHE). And the highest level of the valence band ( $E_{VB}$ ) should be more positive than the redox potential of O<sub>2</sub>/H<sub>2</sub>O (1.23 V vs. NHE) [68]. In order to broaden the photocatalytic applications, 1.00 wt% co-catalyst palladium nanoparticles were decorated on the surface of WTN series and BTN series to increase the electron hole pair separation and thus improve the utilization of the photoinduced electron and hole. For the photocatalytic H<sub>2</sub> generation measurement using Pd-WTN series, the H<sub>2</sub> evolution rates of Pd-WTN-400 are around  $3000 \mu\text{mol}/\text{g h}$  under UV-B irradiation and  $2500 \mu\text{mol}/\text{g h}$  under UV-A irradiation. However, the Pd-WTN series with calcination temperature higher than  $400^\circ\text{C}$  are ineffective for photocatalytic H<sub>2</sub> generation. Because of the particle

size will increase with increasing the calcination temperature, and the large particle size is unfavorable for suspension and thus affect the photocatalytic activity. Fig. 5 presents the photocatalytic H<sub>2</sub> production rates of Pd-WTN-400 and Pd-BTN series. Both Pd-WTN series and Pd-BTN series show the undetectable hydrogen generation value under visible light irradiation. The poor performance is caused by the bandgap of synthesized TiO<sub>2</sub>-based material which is larger than the photon energy of the visible light. As we mentioned above, the photocatalytic H<sub>2</sub> generation belongs to uphill reaction which needs sufficient energy to overcome the large positive change in the Gibbs free energy. Hence, it is difficult to promote the photocatalytic H<sub>2</sub> evolution under visible light irradiation. For white TiO<sub>2</sub> series, Pd-WTN-400 shows the highest H<sub>2</sub> evolution rate among Pd-WTN series. Nevertheless, most samples of Pd-BTN series significantly boost the H<sub>2</sub> evolution rates when they are compared with Pd-WTN-400. Pd-BTN-400 possesses the high photocatalytic hydrogen production, and it approaches  $9300 \mu\text{mol}/\text{g h}$  under UV-B irradiation and  $5200 \mu\text{mol}/\text{g h}$  under UV-A irradiation.

After decorating Pd nanoparticles on the BTN-400 surface by the wet impregnation method, the particle size and crystal structure of Pd-BTN-400 still stand with the original structure. TEM images of BTN-400 and Pd-BTN-400 are shown in Fig. 6. The particle size of BTN-400 ( $\sim 11.3 \pm 1.3 \text{ nm}$ ), and Pd-BTN-400 ( $\sim 11.0 \pm 0.7 \text{ nm}$ ) are almost the same (Fig. 6(a,b)). Fig. 6(c,d) show the high magnification of BTN-400 and Pd-BTN-400. The result also demonstrates that the *d* spacing of (101) crystal plane for BTN-400 ( $\sim 3.48 \text{ \AA}$ ) and Pd-BTN-400 ( $\sim 3.49 \text{ \AA}$ ) are roughly the same. For the distribution of Pd-based nanoparticles on the BTN surface, the average particle diameter is  $\sim 5.6 \pm 0.8 \text{ nm}$ , and it shows a uniform size distribution. The (111) crystal plane of the Pd-based nanoparticles is  $\sim 2.20 \text{ \AA}$ . We also investigated the chemical composition of the BTN-550 and Pd-BTN-550 by XPS analysis. Based on the XPS results summa-

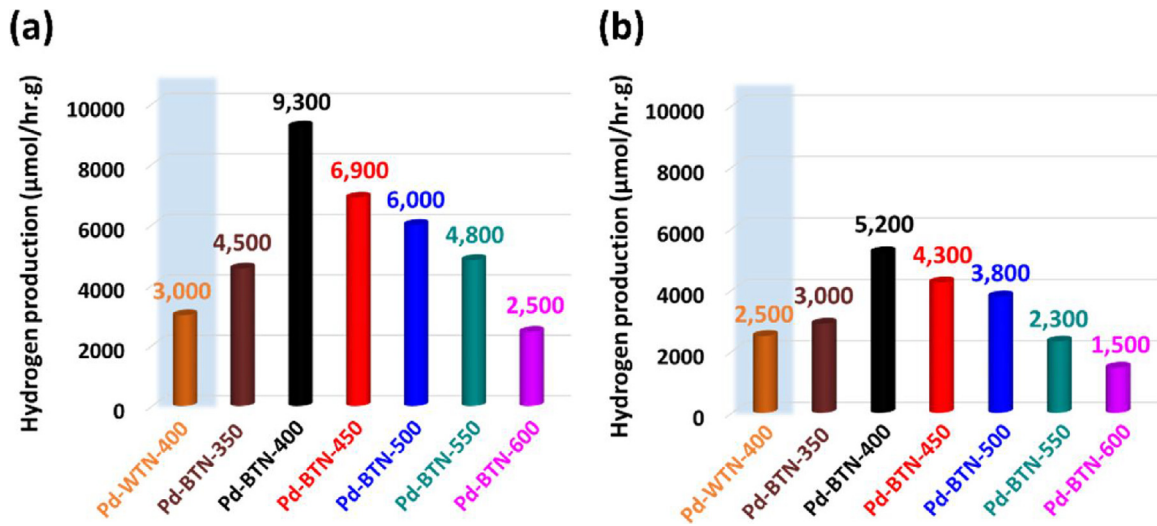


Fig. 5. The hydrogen production rate of various Pd-BTN samples under the following light source irradiation: (a) UV-B and (b) UV-A.

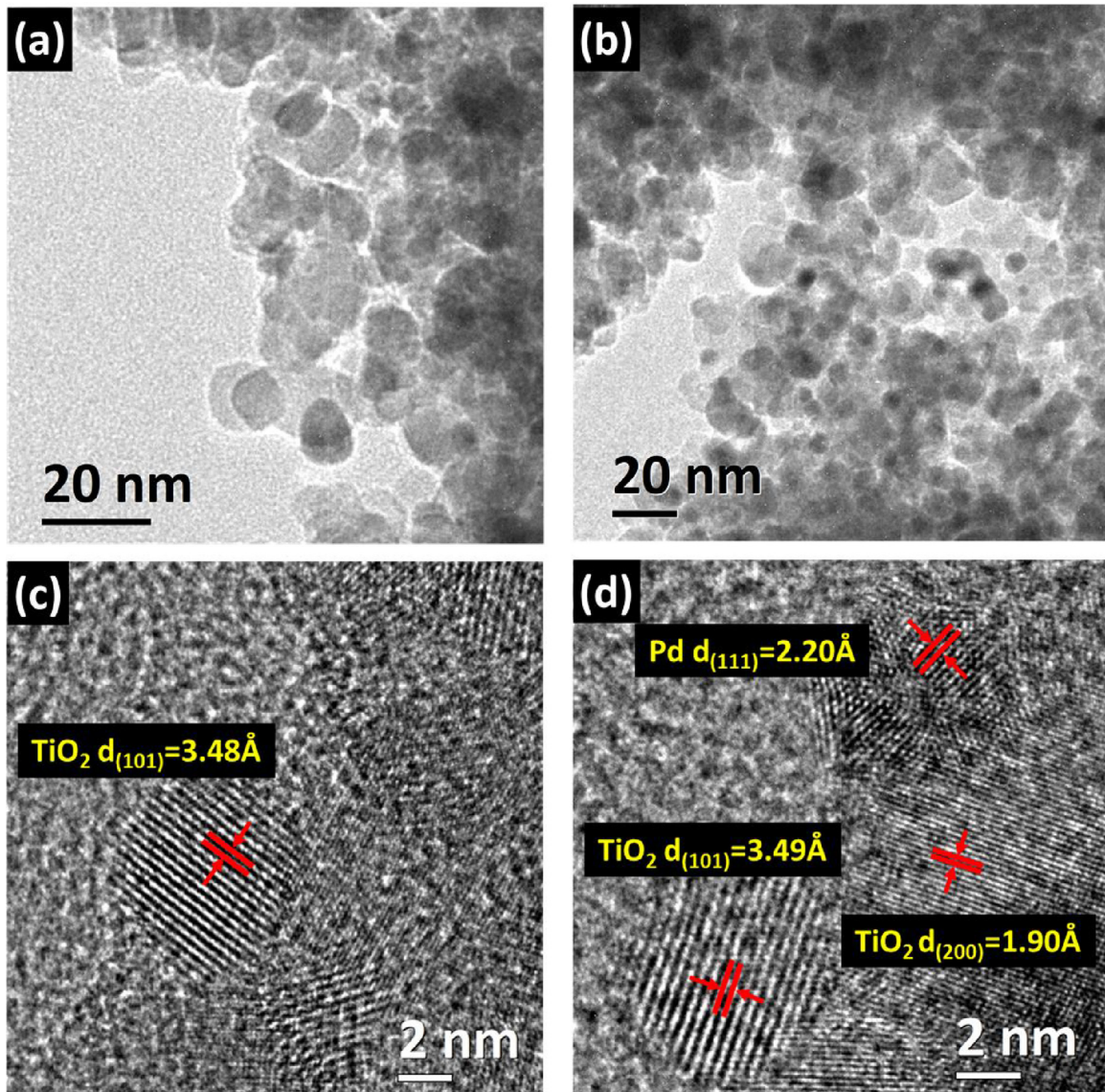


Fig. 6. The high resolution field emission TEM images of (a,c) BTN-400 and (b,d) Pd-BTN-400.

**Table 1**  
XPS peak position and the corresponding atomic ratio of BTN-550 and Pd-BTN-550.

Material	Ti 2p <sub>3/2</sub>		O 1s		Pd 3d	
	BE	Conc.	BE	Conc.	BE	Conc.
	(eV)	(at.%)	(eV)	(at.%)	(eV)	(at.%)
BTN-550	458.9	21.94	530.1	51.98	Not detected	
Pd-BTN-550	458.9	18.69	530.1	50.92	334.9	1.26

**Table 2**  
The ratios of Ti<sup>3+</sup>/Ti, O/Ti, and C/Total of WTN-400, BTN-400, and Pd-BTN-400 calculated by XPS peak-differentiation-imitating analysis.

Sample	Chemical Composition Ratio (%)		
	Ti <sup>3+</sup> /Ti	O/Ti	C/Total
WTN-400	19.49	203.83	15.65
BTN-400	29.15	164.45	12.29
Pd-BTN-400	32.59	242.86	19.48

rized in Table 1, the concentration of Pd-decorated on the surface of Pd-BTN-550 is ~1.26 at.%. We also measured the Kubelka-Munk function,  $F(R)$ , spectra of Pd-BTN series by the UV/Vis spectrophotometer and compared with BTN series as shown in Fig. S3. The  $F(R)$  spectra and camera images indicate that the Pd decoration process will affect the absorption behavior and the color of TiO<sub>2</sub>. After Pd decoration, Pd-BTN-350 and Pd-BTN-400 show the darker brown than BTN-350 and BTN-400. In contrast, for the BTN series with the calcination temperature above 450 °C give the darker black compared with Pd-BTN series. This might be due to the presence of Pd nanoparticles between BTN-400 and BTN-450. Although the Pd decoration process will hinder the absorption behavior, the Pd could enhance the electron-hole separation. Therefore, Pd decoration could enhance the photocatalytic activity [63,69].

Aiming to verify that the black color of BTN is not caused by the existence of carbon, XPS analysis was applied to detect the chemical compositions of WTN-400, BTN-400, and Pd-BTN-400 as shown in Table 2. The XPS spectra, including Ti 2p, O 1s, C 1s, and Pd 3d are shown in Fig. S4. Table 2 indicates that the oxygen concentration of BTN-400 is less than WTN-400. We suggest that while TiO<sub>2</sub> calcined under argon atmosphere, the surrounding with insufficient oxygen could induce oxygen vacancy. The oxygen vacancies tend to form the more titanium trivalent ion (Ti<sup>3+</sup>) in the calcination process [70]. The oxygen concentration of Pd-BTN-400 is higher than WTN-400 and BTN-400 due to the existence of PdO. For O 1s XPS spectra, the Ti–O–H signal (around 531.00 eV) was observed both in WTN-

400 and BTN-400. It shows that the intensity of Ti–O–H signal in BTN-400 is higher than WTN-400. The terminated Ti–O–H bonding located on the BTN-400 surface could be contributed by the oxygen vacancies. The oxygen vacancy defects (Ti<sup>3+</sup> and Ti–O–H terminated bonding) act as the trapped center that catches the photoexcited electron and hole. The existence of the trapped centers could diminish the recombination of electrons and holes efficiently. The carrier lifetime of electron increases from several picoseconds to several nanoseconds [4]. The increasing of carrier lifetime contributes to the enhanced photocatalytic activity of BTN. For C 1s XPS spectra, the ratio of C/Ti for BTN-400 is 12.29% much less than 15.65% of WTN-400. The XPS results indicate that the black color of BTN is caused by the Ti<sup>3+</sup> existence and oxygen vacancy rather than the carbon existence [15,16]. For the Pd chemical state of Pd-BTN-400, the XPS spectrum indicates that Pd and Pd<sup>2+</sup> are the dominant species as shown in Fig. S4(c–4). The ratio of Pd/Pd<sup>2+</sup> is ~53.9/46.1 estimated by XPS peak-differentiation-imitating analysis. From the Raman spectra as shown in Fig. S5, the existence of carbon in BTN also is observed. All samples of BTN series present the typical anatase phase, and its intensity is increased with ascending calcination temperature. The signal of carbon is obviously found in BTN-400. However, with increasing calcination temperature, the signal of carbon is disappeared, which indicated that the carbon was removed and did not exist in BTN during calcination process.

Fig. 7 demonstrates the mechanism of photocatalytic hydrogen evolution over Pd-BTN and the proposed band structure. The photoexcited electron and hole were induced, and they could be captured easily by the surface defect of BTN which serves as an electron trap. The photoexcited electron could transfer from BTN to Pd/PdO because the  $E_{CB}$  levels of TiO<sub>2</sub> ( $E_{CB} = -4.99$  eV vs. vacuum level) is higher than the  $E_{CB}$  levels of PdO ( $E_{CB} = -5.29$  eV vs. vacuum level) and the  $E_F$  level of Pd ( $E_F = -5.22$  eV vs. vacuum level). In the meanwhile, the hole of TiO<sub>2</sub> could transfer to the  $E_{VB}$  level of PdO ( $E_{VB} = -6.29$  eV vs. vacuum level) [71–73]. Moreover, the Schottky interface between the surface defect and Pd/PdO can restrict the electron, and thus extends the lifetime of the electron-hole pairs. With the proper chemical states, the Pd/PdO could catch the electron which could thus diminish the recombination of electron-hole to facilitate the photocatalytic hydrogen generation. Among the synthesized photocatalysts, the H<sub>2</sub> evolution rate of Pd-BTN is ~9300 μmol/g h under UV-B irradiation and ~5200 μmol/g h under UV-A irradiation corresponding to the photon energy conversion efficiency of ~4.12% and ~2.31%. We expect that Pd-BTN shows the higher efficiency for the charge separation than that of Pd-WTN. Pd-

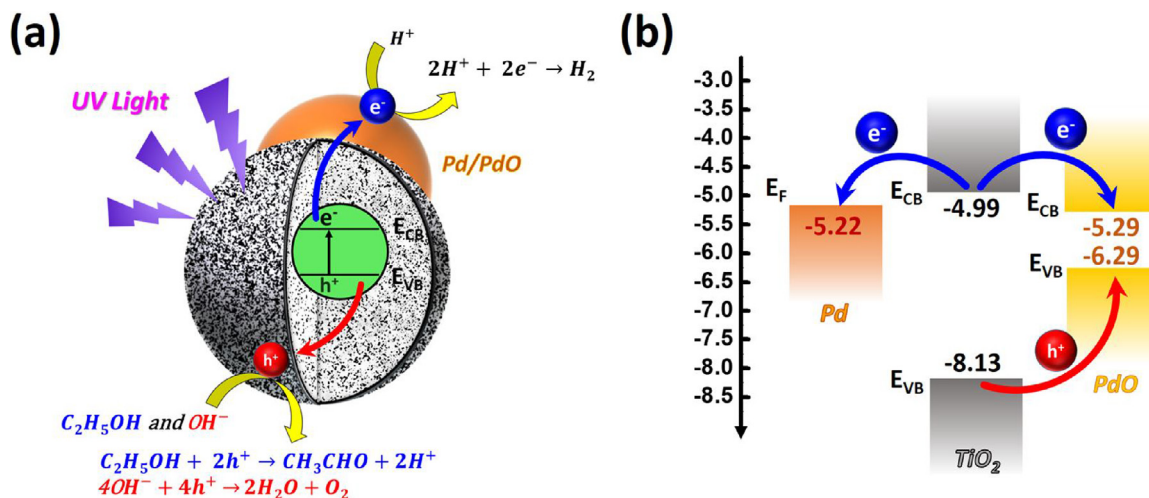


**Fig. 7.** (a) The photocatalytic hydrogen production mechanism and (b) proposed band structure and interfacial charge transfer processes of Pd-BTN.

BTN developed in this study could be applied in the field of green environmental protection and renewable energy.

#### 4. Conclusion

The present study focuses on the preparation of different black TiO<sub>2</sub> nanoparticles by a safe and economical process. The TiO precursor gel was fabricated by sol-gel process. Afterward, a simplified heat treatment in argon is performed to obtain the high-performance BTN photocatalyst. Kubelka-Munk function spectra reveal that BTN-550 has the highest light absorption among the synthesized TiO<sub>2</sub> according to the surface structural defects. BTN-550 thus equips the highest photodegradation activity for methyl orange in all samples. The photodegradation activity is even much higher than the commercial AEROXIDE® TiO<sub>2</sub> P25 under visible light irradiation. Moreover, Pd nanoparticles decorated on the BTN surface can obtain the high photocatalytic hydrogen production rate. The obtained Pd-BTN fulfills a satisfied green material demand in the photocatalytic hydrogen production application. Pd-BTN-400 shows the high photocatalytic H<sub>2</sub> evolution rate of 5200 μmol/g h under UV-A irradiation and 9300 μmol/g h under UV-B irradiation, respectively. The photocatalyst developed by a safe and convenient process is helpful in the society to improve environment issue and make clean energy.

#### Acknowledgements

The authors thank Miss Y.-M. Chang at Instrumentation Centre of National Tsing Hua University for the TEM microstructure analysis and I-Chun Chang at Chang Gung University for the preparation of the material. The authors appreciate Prof. Wei-Fang Su at National Taiwan University and Dr. Ming-Tao Lee at National Synchrotron Radiation Research Centre (BL-13A1) for useful discussion and suggestions. The authors wish to acknowledge the financial support of the Ministry of Science and Technology, Taiwan (MOST 106-2221-E-182-057-MY3, MOST 106-2119-M-002-030, and MOST 105-2632-E-182-001) and Chang Gung Memorial Hospital, Linkou. (CMRPD2E0071, CMRPD2E0072, and BMRPC74).

#### Appendix A. Supplementary data

Supplementary data associated with this article can be found, in the online version, at <http://dx.doi.org/10.1016/j.apsusc.2017.08.071>.

#### References

- [1] A. Kudo, Y. Miseki, Heterogeneous photocatalyst materials for water splitting, *Chem. Soc. Rev.* 38 (2009) 253–278.
- [2] S. Meriam Suhaimy, S. Abd Hamid, C. Lai, M. Hasan, M. Johan, TiO<sub>2</sub> nanotubes supported Cu nanoparticles for improving photocatalytic degradation of simazine under UV illumination, *Catalysts* 6 (2016) 167.
- [3] X. Chen, S.S. Mao, Titanium dioxide nanomaterials: synthesis, properties, modifications, and applications, *Chem. Rev.* 107 (2007) 2891–2959.
- [4] J. Schneider, M. Matsuoka, M. Takeuchi, J. Zhang, Y. Horiuchi, M. Anpo, D.W. Bahnemann, Understanding TiO<sub>2</sub> photocatalysis: mechanisms and materials, *Chem. Rev.* 114 (2014) 9919–9986.
- [5] A. Mohammed, A. Kadhum, M. Ba-Abbad, A. Al-Amiery, Optimization of solar photocatalytic degradation of chloroxylenol using TiO<sub>2</sub> Er<sup>3+</sup>/TiO<sub>2</sub>, and Ni<sup>2+</sup>/TiO<sub>2</sub> via the taguchi orthogonal array technique, *Catalysts* 6 (2016) 163.
- [6] J. Low, B. Cheng, J. Yu, Surface modification and enhanced photocatalytic CO<sub>2</sub> reduction performance of TiO<sub>2</sub>: a review, *Appl. Surf. Sci.* 392 (2017) 658–686.
- [7] C. Xie, S. Yang, J. Shi, C. Niu, Highly crystallized C-doped mesoporous anatase TiO<sub>2</sub> with visible light photocatalytic activity, *Catalysts* 6 (2016) 117.
- [8] M. Ni, M.K.H. Leung, D.Y.C. Leung, K. Sumathy, A review and recent developments in photocatalytic water-splitting using for hydrogen production, *Renewable Sustainable Energy Rev.* 11 (2007) 401–425.
- [9] F. Wu, W. Liu, J. Qiu, J. Li, W. Zhou, Y. Fang, S. Zhang, X. Li, Enhanced photocatalytic degradation and adsorption of methylene blue via TiO<sub>2</sub> nanocrystals supported on graphene-like bamboo charcoal, *Appl. Surf. Sci.* 358 (2015) 425–435.
- [10] D.O. Scanlon, C.W. Dunnill, J. Buckridge, S.A. Shevlin, A.J. Logsdail, S.M. Woodley, C.R.A. Catlow, M.J. Powell, R.G. Palgrave, I.P. Parkin, G.W. Watson, T.W. Keal, P. Sherwood, A. Walsh, A.A. Sokol, Band alignment of rutile and anatase TiO<sub>2</sub>, *Nat. Mater.* 12 (2013) 798–801.
- [11] F. Fresno, R. Portela, S. Suarez, J.M. Coronado, Photocatalytic materials: recent achievements and near future trends, *J. Mater. Chem. A* 2 (2014) 2863–2884.
- [12] X. Chen, L. Liu, P.Y. Yu, S.S. Mao, Increasing solar absorption for photocatalysis with black hydrogenated titanium dioxide nanocrystals, *Science* 331 (2011) 746–750.
- [13] T. Xia, X. Chen, Revealing the structural properties of hydrogenated black TiO<sub>2</sub> nanocrystals, *J. Mater. Chem. A* 1 (2013) 2983–2989.
- [14] J. Zhao, Y. Li, Y. Zhu, Y. Wang, C. Wang, Enhanced CO<sub>2</sub> photoreduction activity of black TiO<sub>2</sub>-coated Cu nanoparticles under visible light irradiation: role of metallic Cu, *Appl. Catal. A* 510 (2016) 34–41.
- [15] A. Ramchiary, S.K. Samdarshi, Hydrogenation based disorder-engineered visible active N-doped mixed phase titania, *Sol. Energy Mater. Sol. Cells* 134 (2015) 381–388.
- [16] Y. Yan, M. Han, A. Konkin, T. Koppe, D. Wang, T. Andreu, G. Chen, U. Vetter, J.R. Morante, P. Schaaf, Slightly hydrogenated TiO<sub>2</sub> with enhanced photocatalytic performance, *J. Mater. Chem. A* 2 (2014) 12708–12716.
- [17] Z. Wang, C. Yang, T. Lin, H. Yin, P. Chen, D. Wan, F. Xu, F. Huang, J. Lin, X. Xie, M. Jiang, H-doped black titania with very high solar absorption and excellent photocatalysis enhanced by localized surface plasmon resonance, *Adv. Funct. Mater.* 23 (2013) 5444–5450.
- [18] E.M. Samsudin, S.B.A. Hamid, J.C. Juan, W.J. Basirun, A.E. Kandjani, Surface modification of mixed-phase hydrogenated TiO<sub>2</sub> and corresponding photocatalytic response, *Appl. Surf. Sci.* 359 (2015) 883–896.
- [19] X. Liu, H. Xu, L.R. Grabstanowicz, S. Gao, Z. Lou, W. Wang, B. Huang, Y. Dai, T. Xu, Ti<sup>3+</sup> self-doped TiO<sub>2-x</sub> anatase nanoparticles via oxidation of TiH<sub>2</sub> in H<sub>2</sub>O<sub>2</sub>, *Catal. Today* 225 (2014) 80–89.
- [20] Z. Wang, C. Yang, T. Lin, H. Yin, P. Chen, D. Wan, F. Xu, F. Huang, J. Lin, X. Xie, M. Jiang, Visible-light photocatalytic, solar thermal and photoelectrochemical properties of aluminium-reduced black titania, *Energy Environ. Sci.* 6 (2013) 3007–3014.
- [21] C. Yang, Z. Wang, T. Lin, H. Yin, X. Lü, D. Wan, T. Xu, C. Zheng, J. Lin, F. Huang, X. Xie, M. Jiang, Core-shell nanostructured black rutile titania as excellent catalyst for hydrogen production enhanced by sulfur doping, *J. Am. Chem. Soc.* 135 (2013) 17831–17838.
- [22] L. Liu, P.Y. Yu, X. Chen, S.S. Mao, D.Z. Shen, Hydrogenation and disorder in engineered black TiO<sub>2</sub>, *Phys. Rev. Lett.* 111 (2013) 065505.
- [23] A. Naldoni, M. Allieta, S. Santangelo, M. Marelli, F. Fabbri, S. Cappelli, C.L. Bianchi, R. Psaro, V. Dal Santo, Effect of nature and location of defects on bandgap narrowing in black TiO<sub>2</sub> nanoparticles, *J. Am. Chem. Soc.* 134 (2012) 7600–7603.
- [24] G. Zhu, T. Lin, X. Lu, W. Zhao, C. Yang, Z. Wang, H. Yin, Z. Liu, F. Huang, J. Lin, Black brookite titania with high solar absorption and excellent photocatalytic performance, *J. Mater. Chem. A* 1 (2013) 9650–9653.
- [25] M.-C. Wu, I.C. Chang, K.-C. Hsiao, W.-K. Huang, Highly visible-light absorbing black TiO<sub>2</sub> nanocrystals synthesized by sol-gel method and subsequent heat treatment in low partial pressure H<sub>2</sub>, *J. Taiwan Inst. Chem. Eng.* 63 (2016) 430–435.
- [26] T. Lin, C. Yang, Z. Wang, H. Yin, X. Lu, F. Huang, J. Lin, X. Xie, M. Jiang, Effective nonmetal incorporation in black titania with enhanced solar energy utilization, *Energy Environ. Sci.* 7 (2014) 967–972.
- [27] G. Wang, H. Wang, Y. Ling, Y. Tang, X. Yang, R.C. Fitzmorris, C. Wang, J.Z. Zhang, Y. Li, Hydrogen-treated TiO<sub>2</sub> nanowire arrays for photoelectrochemical water splitting, *Nano Lett.* 11 (2011) 3026–3033.
- [28] H. Cui, W. Zhao, C. Yang, H. Yin, T. Lin, Y. Shan, Y. Xie, H. Gu, F. Huang, Black TiO<sub>2</sub> nanotube arrays for high-efficiency photoelectrochemical water-splitting, *J. Mater. Chem. A* 2 (2014) 8612–8616.
- [29] X. Li, J. Yu, J. Low, Y. Fang, J. Xiao, X. Chen, Engineering heterogeneous semiconductors for solar water splitting, *J. Mater. Chem. A* 3 (2015) 2485–2534.
- [30] C.W. Dunnill, Z. Ansari, A. Kafizas, S. Perni, D.J. Morgan, M. Wilson, I.P. Parkin, Visible light photocatalysts-N-doped TiO<sub>2</sub> by sol-gel, enhanced with surface bound silver nanoparticle islands, *J. Mater. Chem.* 21 (2011) 11854–11861.
- [31] M.-C. Wu, J. Hiltunen, A. Sapi, A. Avila, W. Larsson, H.-C. Liao, M. Huuhtanen, G. Toth, A. Shchukarev, N. Laufer, . Kukovecz, Z. Konya, J.-P. Mikkola, R. Keiski, W.-F. Su, Y.-F. Chen, H. Jantunen, P.M. Ajayan, R. Vajtai, K. Kordas, Nitrogen-doped anatase nanofibers decorated with noble metal nanoparticles for photocatalytic production of hydrogen, *ACS Nano* 5 (2011) 5025–5030.
- [32] M.-C. Wu, H.-C. Liao, Y.-C. Cho, G. Toth, Y.-F. Chen, W.-F. Su, K. Kordas, Photo-kelvin probe force microscopy for photocatalytic performance characterization of single filament of TiO<sub>2</sub> nanofiber photocatalysts, *J. Mater. Chem. A* 1 (2013) 5715–5720.
- [33] S. Xu, J. Ng, X. Zhang, H. Bai, D.D. Sun, Fabrication and comparison of highly efficient Cu incorporated TiO<sub>2</sub> photocatalyst for hydrogen generation from water, *Int. J. Hydrogen Energy* 35 (2010) 5254–5261.
- [34] T. Huang, S. Mao, J. Yu, Z. Wen, G. Lu, J. Chen, Effects of N and F doping on structure and photocatalytic properties of anatase TiO<sub>2</sub> nanoparticles, *RSC Adv.* 3 (2013) 16657–16664.
- [35] X. Jiang, X. Fu, L. Zhang, S. Meng, S. Chen, Photocatalytic reforming of glycerol for H<sub>2</sub> evolution on Pt/TiO<sub>2</sub>: fundamental understanding the effect of co-catalyst Pt and the Pt deposition route, *J. Mater. Chem. A* 3 (2015) 2271–2282.

- [36] T. Liu, H. Zhang, Novel Fe-doped anatase TiO<sub>2</sub> nanosheet hierarchical spheres with 94% {001} facets for efficient visible light photodegradation of organic dye, *RSC Adv.* 3 (2013) 16255–16258.
- [37] A. Pandikumar, K. Sivaranjani, C.S. Gopinath, R. Ramaraj, Aminosilicate sol-gel stabilized N-doped TiO<sub>2</sub>-Au nanocomposite materials and their potential environmental remediation applications, *RSC Adv.* 3 (2013) 13390–13398.
- [38] G. Pórtári, D. Madarász, L. Nagy, B. László, A. Sápi, A. Oszkó, A. Kukovec, A. Erdőhelyi, Z. Kónya, J. Kiss, Rh-induced support transformation phenomena in titanate nanowire and nanotube catalysts, *Langmuir* 29 (2013) 3061–3072.
- [39] X. Zhang, J. Yao, D. Li, X. Chen, H. Wang, L.Y. Yeo, J.R. Friend, Self-assembled highly crystalline TiO<sub>2</sub> mesostructures for sunlight-driven, pH-responsive photodegradation of dyes, *Mater. Res. Bull.* 55 (2014) 13–18.
- [40] S. Xu, A.J. Du, J. Liu, J. Ng, D.D. Sun, Highly efficient CuO incorporated TiO<sub>2</sub> nanotube photocatalyst for hydrogen production from water, *Int. J. Hydrogen Energy* 36 (2011) 6560–6568.
- [41] M.S. Akple, J. Low, S. Wageh, A.A. Al-Ghamdi, J. Yu, J. Zhang, Enhanced visible light photocatalytic H<sub>2</sub>-production activity of g-C<sub>3</sub>N<sub>4</sub>/WS<sub>2</sub> composite heterostructures, *Appl. Surf. Sci.* 358 (2015) 196–203.
- [42] L.J. Zhang, R. Zheng, S. Li, B.K. Liu, D.J. Wang, L.L. Wang, T.F. Xie, Enhanced photocatalytic H<sub>2</sub> generation on cadmium sulfide nanorods with cobalt hydroxide as cocatalyst and insights into their photogenerated charge transfer properties, *ACS Appl. Mater. Interfaces* 6 (2014) 13406–13412.
- [43] D. Lang, F. Cheng, Q. Xiang, Enhancement of photocatalytic H<sub>2</sub> production activity of CdS nanorods by cobalt-based cocatalyst modification, *Catal. Sci. Technol.* 6 (2016) 6207–6216.
- [44] T. Jia, A. Kolpin, C. Ma, R.C.-T. Chan, W.-M. Kwok, S.C.E. Tsang, A graphene dispersed CdS-MoS<sub>2</sub> nanocrystal ensemble for cooperative photocatalytic hydrogen production from water, *Chem. Commun.* 50 (2014) 1185–1188.
- [45] Q. Xiang, F. Cheng, D. Lang, Hierarchical layered WS<sub>2</sub>/graphene-modified CdS nanorods for efficient photocatalytic hydrogen evolution, *ChemSusChem* 9 (2016) 996–1002.
- [46] J. Low, J. Yu, M. Jaroniec, S. Wageh, A.A. Al-Ghamdi, Heterojunction photocatalysts, *Adv. Mater.* 29 (2017) 1601694.
- [47] P. Wang, Y. Lu, X. Wang, H. Yu, Co-modification of amorphous-Ti(IV) hole cocatalyst and Ni(OH)<sub>2</sub> electron cocatalyst for enhanced photocatalytic H<sub>2</sub>-production performance of TiO<sub>2</sub>, *Appl. Surf. Sci.* 391 (2017) 259–266.
- [48] A. Meng, J. Zhang, D. Xu, B. Cheng, J. Yu, Enhanced photocatalytic H<sub>2</sub>-production activity of anatase TiO<sub>2</sub> nanosheet by selectively depositing dual-cocatalysts on {101} and {001} facets, *Appl. Catal. B* 198 (2016) 286–294.
- [49] B. Tahir, M. Tahir, N.S. Amin, Gold–indium modified TiO<sub>2</sub> nanocatalysts for photocatalytic CO<sub>2</sub> reduction with H<sub>2</sub> as reductant in a monolith photoreactor, *Appl. Surf. Sci.* 338 (2015) 1–14.
- [50] L. Clarizia, I.D. Somma, L. Onotri, R. Andreozzi, R. Marotta, Kinetic modeling of hydrogen generation over nano-Cu(s)/TiO<sub>2</sub> catalyst through photoreforming of alcohols, *Catal. Today* 281 (2017) 117–123.
- [51] D. Xu, Y. Hai, X. Zhang, S. Zhang, R. He, Bi<sub>2</sub>O<sub>3</sub> cocatalyst improving photocatalytic hydrogen evolution performance of TiO<sub>2</sub>, *Appl. Surf. Sci.* 400 (2017) 530–536.
- [52] Z. He, J. Fu, B. Cheng, J. Yu, S. Cao, Cu<sub>2</sub>(OH)<sub>2</sub>CO<sub>3</sub> clusters: novel noble-metal-free cocatalysts for efficient photocatalytic hydrogen production from water splitting, *Appl. Catal. B* 205 (2017) 104–111.
- [53] J. Zheng, S. Bao, X. Zhang, H. Wu, R. Chen, P. Jin, Pd–MgNi<sub>x</sub> nanospheres/black-TiO<sub>2</sub> porous films with highly efficient hydrogen production by near-complete suppression of surface recombination, *Appl. Catal. B* 183 (2016) 69–74.
- [54] S. Min, J. Hou, Y. Lei, X. Ma, G. Lu, Facile one-step hydrothermal synthesis toward strongly coupled TiO<sub>2</sub>/graphene quantum dots photocatalysts for efficient hydrogen evolution, *Appl. Surf. Sci.* 396 (2017) 1375–1382.
- [55] S. Bera, J.E. Lee, S.B. Rawal, W.I. Lee, Size-dependent plasmonic effects of Au and Au@SiO<sub>2</sub> nanoparticles in photocatalytic CO<sub>2</sub> conversion reaction of Pt/TiO<sub>2</sub>, *Appl. Catal. B* 199 (2016) 55–63.
- [56] E. Kazuma, T. Tatsuma, Localized surface plasmon resonance sensors based on wavelength-tunable spectral dips, *Nanoscale* 6 (2014) 2397–2405.
- [57] Z. Lin, X. Wang, J. Liu, Z. Tian, L. Dai, B. He, C. Han, Y. Wu, Z. Zeng, Z. Hu, On the role of localized surface plasmon resonance in UV–vis light irradiated Au/TiO<sub>2</sub> photocatalysis systems: pros and cons, *Nanoscale* 7 (2015) 4114–4123.
- [58] J. Fang, S.-W. Cao, Z. Wang, M.M. Shahjamali, S.C.J. Loo, J. Barber, C. Xue, Mesoporous plasmonic Au–TiO<sub>2</sub> nanocomposites for efficient visible-light-driven photocatalytic water reduction, *Int. J. Hydrogen Energy* 37 (2012) 17853–17861.
- [59] Y. Wang, J. Yu, W. Xiao, Q. Li, Microwave-assisted hydrothermal synthesis of graphene based Au–TiO<sub>2</sub> photocatalysts for efficient visible-light hydrogen production, *J. Mater. Chem. A* 2 (2014) 3847–3855.
- [60] X. Chen, L. Liu, Z. Liu, M.A. Marcus, W.-C. Wang, N.A. Olyler, M.E. Grass, B. Mao, P.-A. Glans, P.Y. Yu, J. Guo, S.S. Mao, Properties of disorder-engineered black titanium dioxide nanoparticles through hydrogenation, *Sci. Rep.* 3 (2013) 1510.
- [61] X. Chen, L. Liu, F. Huang, Black titanium dioxide (TiO<sub>2</sub>) nanomaterials, *Chem. Soc. Rev.* 44 (2015) 1861–1885.
- [62] K. Maeda, K. Domen, New non-oxide photocatalysts designed for overall water splitting under visible light, *J. Phys. Chem. C* 111 (2007) 7851–7861.
- [63] M.-C. Wu, I.-C. Chang, W.-K. Huang, Y.-C. Tu, C.-P. Hsu, W.-F. Su, Correlation between palladium chemical state and photocatalytic performance of TiO<sub>2</sub>-Pd based nanoparticles, *Thin Solid Films* 570 (2014) 371–375.
- [64] M. Rezaee, S.M. Mousavi Khoie, K.H. Liu, The role of brookite in mechanical activation of anatase-to-rutile transformation of nanocrystalline TiO<sub>2</sub>: an XRD and raman spectroscopy investigation, *CrystEngComm* 13 (2011) 5055–5061.
- [65] A. Katti, S.R. Venna, M.A. Carreon, Self-assembly hydrothermal assisted synthesis of mesoporous anatase in the presence of ethylene glycol, *Catal. Commun.* 10 (2009) 2036–2040.
- [66] M.-C. Wu, J.-S. Chih, W.-K. Huang, Bismuth doping effect on TiO<sub>2</sub> nanofibers for morphological change and photocatalytic performance, *CrystEngComm* 16 (2014) 10692–10699.
- [67] K.J.A. Raj, B. Viswanathan, Effect of surface area, pore volume and particle size of P25 titania on the phase transformation of anatase to rutile, *Indian J. Chem., Sect. A* 48 (2009) 1378–1382.
- [68] T. Hisatomi, J. Kubota, K. Domen, Recent advances in semiconductors for photocatalytic and photoelectrochemical water splitting, *Chem. Soc. Rev.* 43 (2014) 7520–7535.
- [69] M.-C. Wu, P.-H. Lee, D.-L. Lee, Enhanced photocatalytic activity of palladium decorated TiO<sub>2</sub> nanofibers containing anatase-rutile mixed phase, *Int. J. Hydrogen Energy* 40 (2015) 4558–4566.
- [70] X. Pan, M.-Q. Yang, X. Fu, N. Zhang, Y.-J. Xu, Defective TiO<sub>2</sub> with oxygen vacancies: synthesis, properties and photocatalytic applications, *Nanoscale* 5 (2013) 3601–3614.
- [71] W. Zhou, Y. Guan, D. Wang, X. Zhang, D. Liu, H. Jiang, J. Wang, X. Liu, H. Liu, S. Chen, PdO/TiO<sub>2</sub> and Pd/TiO<sub>2</sub> heterostructured nanobelts with enhanced photocatalytic activity, *Chem. Asian J.* 9 (2014) 1648–1654.
- [72] Y.-H. Chiu, Y.-J. Hsu, Au@Cu<sub>7</sub>S<sub>4</sub> yolk@shell nanocrystal-decorated TiO<sub>2</sub> nanowires as an all-day-active photocatalyst for environmental purification, *Nano Energy* 31 (2017) 286–295.
- [73] M.-C. Wu, C.-H. Chen, W.-K. Huang, K.-C. Hsiao, T.-H. Lin, S.-H. Chan, P.-Y. Wu, C.-F. Lu, Y.-H. Chang, T.-F. Lin, K.-H. Hsu, J.-F. Hsu, K.-M. Lee, J.-J. Shyue, K. Kordás, W.-F. Su, Improved solar-driven photocatalytic performance of highly crystalline hydrogenated TiO<sub>2</sub> nanofibers with core-shell structure, *Sci. Rep.* 7 (2017) 40896.